

The 100,000-Year Ice-Age Cycle Identified and Found to Lag Temperature, Carbon Dioxide, and Orbital Eccentricity

Nicholas J. Shackleton

Science 289, 1897 (2000);

DOI: 10.1126/science.289.5486.1897

This copy is for your personal, non-commercial use only.

If you wish to distribute this article to others, you can order high-quality copies for your colleagues, clients, or customers by [clicking here](#).

Permission to republish or repurpose articles or portions of articles can be obtained by following the guidelines [here](#).

The following resources related to this article are available online at www.sciencemag.org (this information is current as of December 8, 2010):

Updated information and services, including high-resolution figures, can be found in the online version of this article at:

<http://www.sciencemag.org/content/289/5486/1897.full.html>

A list of selected additional articles on the Science Web sites **related to this article** can be found at:

<http://www.sciencemag.org/content/289/5486/1897.full.html#related>

This article **cites 26 articles**, 7 of which can be accessed free:

<http://www.sciencemag.org/content/289/5486/1897.full.html#ref-list-1>

This article has been **cited by** 363 article(s) on the ISI Web of Science

This article has been **cited by** 36 articles hosted by HighWire Press; see:

<http://www.sciencemag.org/content/289/5486/1897.full.html#related-urls>

This article appears in the following **subject collections**:

Atmospheric Science

<http://www.sciencemag.org/cgi/collection/atmos>

The 100,000-Year Ice-Age Cycle Identified and Found to Lag Temperature, Carbon Dioxide, and Orbital Eccentricity

Nicholas J. Shackleton

The deep-sea sediment oxygen isotopic composition ($\delta^{18}\text{O}$) record is dominated by a 100,000-year cyclicity that is universally interpreted as the main ice-age rhythm. Here, the ice volume component of this $\delta^{18}\text{O}$ signal was extracted by using the record of $\delta^{18}\text{O}$ in atmospheric oxygen trapped in Antarctic ice at Vostok, precisely orbitally tuned. The benthic marine $\delta^{18}\text{O}$ record is heavily contaminated by the effect of deep-water temperature variability, but by using the Vostok record, the $\delta^{18}\text{O}$ signals of ice volume, deep-water temperature, and additional processes affecting air $\delta^{18}\text{O}$ (that is, a varying Dole effect) were separated. At the 100,000-year period, atmospheric carbon dioxide, Vostok air temperature, and deep-water temperature are in phase with orbital eccentricity, whereas ice volume lags these three variables. Hence, the 100,000-year cycle does not arise from ice sheet dynamics; instead, it is probably the response of the global carbon cycle that generates the eccentricity signal by causing changes in atmospheric carbon dioxide concentration.

It has long been apparent that there is an ~100,000-year (100-ky) cyclicity in $\delta^{18}\text{O}$ records from deep-sea cores. The first evidence for the duration of these cycles came from the use of radiometric dates from uplifted corals on the island of Barbados as a tool for dating the marine $\delta^{18}\text{O}$ record (1). The second piece of evidence arose from anchoring the older part of the sequence of cycles to the radiometrically dated Brunhes-Matuyama magnetic polarity reversal (2). It is generally accepted that this 100-ky cycle represents a major component of the record of changes in total Northern Hemisphere ice volume (3). It is difficult to explain this predominant cycle in terms of orbital eccentricity because “the 100,000-year radiation cycle (arising from eccentricity variations) is much too small in amplitude and too late in phase to produce the corresponding climatic cycle by direct forcing” (4, p. 700). Most published explanations for the large amount of ice volume variability at this wavelength draw on the long response time that is associated with large ice sheets (5), especially when the response time of the underlying bedrock is taken into account. Imbrie and Imbrie (6) devised a simple mathematical model in which the slow and nonlinear response of a major ice sheet could generate an ice volume response with the 100-ky period of orbital eccentricity when the precession-dominated 65°N summer insolation record is used as a forcing. The nonlinearity of the ice sheet response (rapid degla-

ciation but slow ice growth) is an essential contribution to the relative success of this model.

It is difficult to test the proposed mechanisms for explaining the 100-ky cycle for several reasons. In particular, the strong 100-ky cycle has only dominated paleoclimate variability over about the past million years, too short a period to rigorously investigate with time-series analysis. Alternative explanations that have been proposed include forcing by orbital inclination (7) (which has a single 100-ky period, in contrast to the mixture of 95 and 125 ky that characterizes orbital eccentricity) and a wide range of models [reviewed in (4)] that seek to generate this cycle with or without the possibility of free oscillations. None of these investigations have questioned the primary association of the 100-ky $\delta^{18}\text{O}$ cycle with global ice volume.

The time scale for the records that are used for the investigation of the 100-ky cycle is based on the existence in these $\delta^{18}\text{O}$ records of variability that is confidently associated with variations in axial obliquity (41 ky) and with the precession of the equinoxes (23 and 19 ky) (8). Within the SPECMAP project (9, 10), a time scale was developed for the marine $\delta^{18}\text{O}$ record that is based on locking the phase of the observed cycles to an orbital template. The validity of this time scale is supported by the convincing coherence between marine $\delta^{18}\text{O}$ (and other climate-related proxies) and the assumed obliquity and precession forcings. With these astronomically based age models, the 100-ky portion of the variability is significantly co-

herent with orbital eccentricity, but the coherence is not overwhelming. Given the difficulty in successfully explaining the 100-ky signal (4), doubts remain regarding its association with orbital eccentricity.

Atmospheric oxygen exchanges isotopically with the oxygen in ocean water chiefly as a consequence of global photosynthesis. The $\delta^{18}\text{O}$ of atmospheric oxygen differs from that of the ocean by ~23.5 per mil (%); this difference is known as the Dole effect, and its origin is reviewed in (11). The record of $\delta^{18}\text{O}$ of atmospheric oxygen trapped in bubbles in the polar ice sheets must reflect changes in marine $\delta^{18}\text{O}$ with a small delay that is controlled by the balance between the rate of total global photosynthesis and the size of the atmospheric oxygen reservoir (12). Bender *et al.* (11) evaluated this balance and derived a turnover time of ~1 ky. Here, the 100-ky component of the atmospheric $\delta^{18}\text{O}$ signal is investigated. This proves to shed light on the 100-ky signal in marine $\delta^{18}\text{O}$.

A time scale for the atmospheric gas record from Vostok. Petit *et al.* (13) published 400-ky-long records of three signals embedded in the air bubbles of the Vostok ice cores. The concentrations of CO_2 and CH_4 are particularly interesting because these are both important greenhouse gases. The third record is of the $\delta^{18}\text{O}$ of atmospheric oxygen, which varies in response to the $\delta^{18}\text{O}$ of ocean water as noted above and to changes in the conditions of global terrestrial photosynthesis and other factors that change the magnitude of the Dole effect (11). Petit *et al.* (13) illustrated the obvious similarity between the $\delta^{18}\text{O}$ of atmospheric oxygen on their time scale and 65°N summer insolation (Fig. 1A) but did not generate a new time scale based on this comparison.

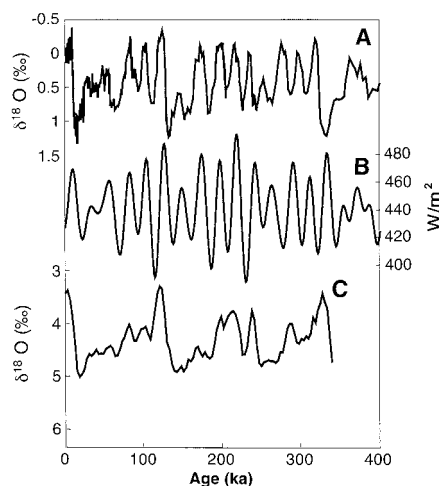


Fig. 1. (A) Vostok air $\delta^{18}\text{O}$ record of (13), published time scale. (B) The “classic” Milankovitch forcing, June insolation at 65°N. (C) Benthic $\delta^{18}\text{O}$ record of core V19-30 (18), published time scale.

Sowers *et al.* (12) generated a time scale for the upper part of the Vostok core by correlating their record of air $\delta^{18}\text{O}$ (at that time extending to ~ 130 ky) to the SPECMAP time scale (10). Instead of taking this approach, the similarity between Fig. 1A and 1B [noted in (13)] was used here to generate a more refined time scale that is independent of SPECMAP (10). The advantage of this approach is that the strong amplitude modulation of the precession forcing provides a very powerful criterion for judging the success of the time scale where there is a precession-related signal (14). None of the records used in constructing the SPECMAP time scale (10) contain such a “clean” precession signal; therefore, it appears likely that this procedure will lead to a more accurate time scale than could be achieved by correlating to SPECMAP. In order to determine the phase of the record relative to precession, an independent age is required for at least one event. The upper part of the Greenland Ice Sheet Project 2 ice core has an age scale that is based on annual layer counting and is accurate to better than $\pm 2\%$ (15); the record of $\delta^{18}\text{O}$ of atmospheric oxygen in this core (16) shows that the age of the midpoint of the most recent glacial-to-interglacial transition is 12,000 years ago (12 ka). The phase lags in the tuning target, 5 ky for precession and 8 ky for obliquity, are determined so as to be consistent with this age (once the precession phase is set, the phase relative to obliquity is determined by the record itself). In the final tuning target, the amplitudes of the precession and obliquity components are matched to their coherent amplitudes in the record. Steps in the processing of the time series are

available as supplemental Web material (17). To minimize “spikes” in the differences between pairs of records, tuning was carried out by assigning ages to the midpoints of transitions; Web table 1 (17) gives the published and tuned transition ages. The data on the new time scale, together with the tuning target, are shown in Fig. 2.

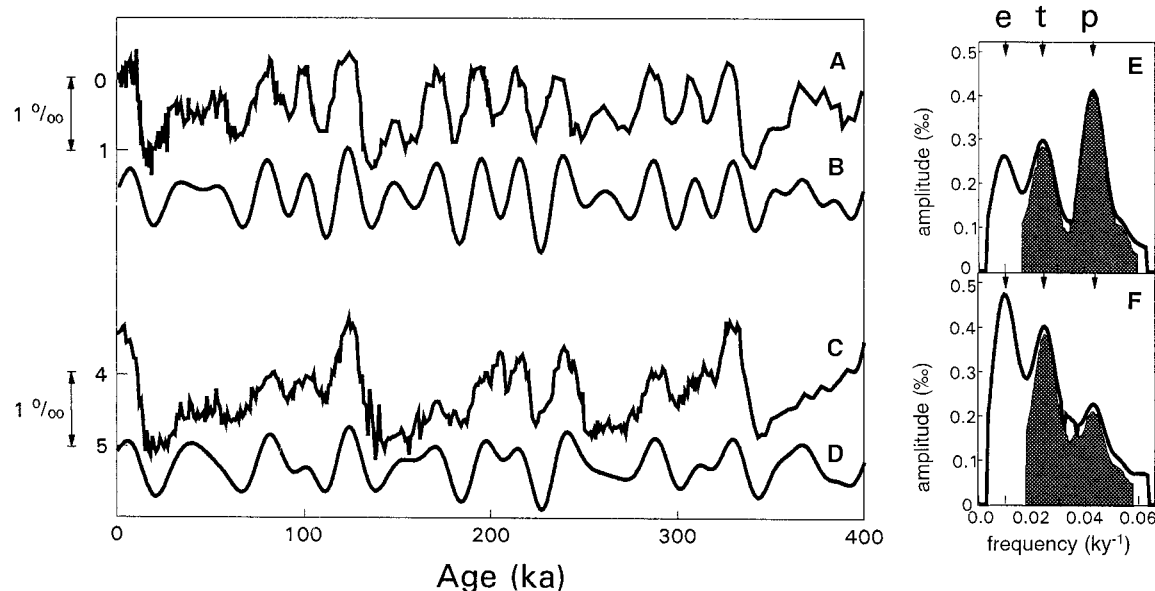
A new time scale for the benthic marine $\delta^{18}\text{O}$ record. In order to construct a strictly comparable deep-sea chronology, the well-known benthic foraminiferal $\delta^{18}\text{O}$ record of core V19-30 (18) was retuned by using a procedure analogous to that described above. The V19-30 record was slightly extended by using the data from nearby core V19-28 (19) to make a high-quality record of the same length as the Vostok record. In designing the final tuning target for V19-30, an account was taken of the fact that the target (and hence the tuned data) should lead rather than lag the Vostok target, because the Vostok air $\delta^{18}\text{O}$ record must incorporate the history of the changing marine $\delta^{18}\text{O}$ record with an ~ 1 -ky lag (11). In order to satisfy this requirement, the modeled midpoint of the last deglaciation must be 13 ka, yielding lags of 3 ky with respect to precession and 7 ky with respect to obliquity. The V19-30 (extended) record on this time scale is shown in Fig. 2C, together with its tuning target. This time scale is very similar (20) to that already published but differs in detail because the record was tuned directly to a specially designed orbital target instead of being tuned with SPECMAP age controls (10) and also because only transition midpoints were used for age controls, rather than a mixture of controls. The amplitudes and coherent amplitudes and the phase

lags in the obliquity and precession bands of the two records after this tuning are given in Table 1.

In the time scales developed under the inspiration of Imbrie (8, 9), the assumption was made that the phase lags with respect to obliquity and precession ought to reflect the lag of a single-exponent system with a reasonable time constant for the response of a continental ice sheet. In the present work, this requirement was relaxed because it is now known that there are a number of different components contributing to the $\delta^{18}\text{O}$ records, each with a different time constant. The approach whereby the tuning target is optimized to the data enables the difference (in thousands of years) between the lags with respect to the obliquity and precession components of midsummer insolation to be estimated; geological ages for the last deglaciation then give the absolute lags.

Comparing the Vostok air $\delta^{18}\text{O}$ record and the benthic marine $\delta^{18}\text{O}$ record. The linear variance spectra of the air and benthic $\delta^{18}\text{O}$ records obtained by cross-spectral analysis versus their respective orbital tuning targets are also shown in Fig. 2 (21). In view of the relatively short (~ 1 ky) turnover time of atmospheric oxygen with respect to marine photosynthesis (11), the amplitude of the marine $\delta^{18}\text{O}$ signal must be fully captured by the air $\delta^{18}\text{O}$ record, yet at the obliquity frequency, the foraminiferal signal is clearly larger. This demonstrates that a substantial part of the foraminiferal obliquity signal ($\sim 0.12\%$ coherent amplitude) must derive from changing deep-ocean temperature, which affects the isotopic fractionation between water and carbonate, and not from ice volume. On the

Fig. 2. (A) Vostok air $\delta^{18}\text{O}$ record (13), on the tuned time scale of this paper. (B) Tuning target for the Vostok air $\delta^{18}\text{O}$ record. (C) Benthic $\delta^{18}\text{O}$ record of cores V19-30 and V19-28 on the tuned time scale of this paper. (D) Tuning target for the V19-30/V19-28 benthic $\delta^{18}\text{O}$ record. (E) Linear variance amplitude spectrum for the air $\delta^{18}\text{O}$ record, obtained by cross-spectral analysis versus its tuning target; the shaded area illustrates the amplitude of coherent variance in the obliquity and precession bands (the tuning targets do not include eccentricity). (F) Linear variance amplitude spectrum for the benthic $\delta^{18}\text{O}$ record, obtained by cross-spectral analysis versus its tuning target; the shaded area illustrates the amplitude of coherent variance in the obliquity and precession



bands (the tuning targets do not include eccentricity). Arrows labeled “e,” “t,” and “p” identify the frequencies associated with eccentricity, obliquity (tilt), and precession.

other hand, in the precession band it is evident that almost half of the signal recorded in air $\delta^{18}\text{O}$ must arise from changes in the Dole effect, because at this frequency the air $\delta^{18}\text{O}$ signal is twice the amplitude of the foraminiferal $\delta^{18}\text{O}$ signal (22). It is clear from the elegant and thorough review by Bender *et al.* (11) that there are many potential routes through which this could arise. However, the extremely high coherence with precession (see Table 1) suggests that there must be a relatively simple dominating mechanism that yields an almost linear response. Although part of the phase lag undoubtedly reflects the 1-ky response of the atmosphere with respect to photosynthesis, the remainder implies either a mechanism for changing the Dole effect that has a long time constant (which is unlikely) or control centered on a time of year that is later than midsummer. A relation with varying monsoon precipitation was suggested in (11), and both modeling and observation suggest that the monsoon precipitation lags the orbital forcing by a few thousand years (23), equivalent to an autumn response.

The precession component in air $\delta^{18}\text{O}$ must be composed of an ice volume signal and a Dole effect signal. Because these two must have approximately the same absolute phase, the amplitudes may be subtracted without complication, yielding a maximum amplitude of 0.22‰ for ice volume and a minimum of 0.21‰ relating to the Dole effect. These values are adopted in the following discussion in the knowledge that if a higher value is assigned, the implication would be a reduced precession component allocated to ice volume variability, in which case a part of the precession-related variability in the V19-30 record would be reallocated to changing deep-water temperature. The best way to refine this partitioning will be to accurately determine the sea levels at ~90 and 110 ka in comparison with levels at ~80 and 100 ka, because these differences reflect the precession contribution to sea level variability.

It is impossible at present to analytically determine whether any of the 41-ky variance in the air $\delta^{18}\text{O}$ signal is attributable to the Dole effect or whether it derives from the ocean water. However, if it is assumed that the precession variance in the Dole effect is

related to monsoon precipitation, then there ought to be an obliquity component that is commensurate with the contribution of obliquity to the low-latitude insolation spectrum. In the region and season of the Indian monsoon, the proportion of variance arising from obliquity is ~10% of the total, equivalent to an amplitude of ~0.02‰, which is negligible in relation to the overall 0.27‰ coherent amplitude associated with obliquity.

The residual signal and eccentricity. It has been shown that almost all of the 41- and 21-ky variance in the air $\delta^{18}\text{O}$ signal can be explained as a linear response to orbital forcing. The result of subtracting this linearly forced component (24) from the observed record is shown in Fig. 3A. The equivalent for the V19-30 foraminiferal $\delta^{18}\text{O}$ record, obtained by subtracting the linearly forced component of the 41- and 21-ky variance from the full record is shown in Fig. 3B. Three features stand out. First, both residuals display the 100-ky cycle; second, the amplitude of this signal is far smaller in the Vostok atmospheric $\delta^{18}\text{O}$ residual than in the V19-30 foraminiferal $\delta^{18}\text{O}$ residual; and third, the residuals retain “jumps” in value at deglaciations, such as at the base of the Holocene (12 ka) and at the base of marine isotope stage (MIS) 5 (128 ka).

With regard to the first observation, cross-

spectral analysis versus eccentricity, tilt, and precession (ETP) parameters (25) shows that, in both cases, the residual is coherent with eccentricity with small, but different, phase lags. However, the records are too short to attach much importance to this observation on its own.

It is difficult to conceive of a mechanism that would prevent the atmospheric $\delta^{18}\text{O}$ recording the full amplitude of a 100-ky cycle in ocean water $\delta^{18}\text{O}$; thus, the implication of the second observation must be that a substantial portion of the marine 100-ky cycle that has been the object of so much attention over the past quarter of a century is, in reality, a deep-water temperature signal and not an ice volume signal.

The third observation confirms the supposition that the rapid deglacial “terminations” cannot be explained as part of the linear response of the climate system (4). This observation has the important implication that the midpoint of the transition in a linear target cannot be expected to predict the exact age of the midpoint of one of these deglaciations (26). On the other hand, the rapid nonlinear part of the transition must have been close to this midpoint, or the residual would show an anomalous overshoot. Experiments were conducted to determine the oldest allowable base for the last interglacial that is consistent with

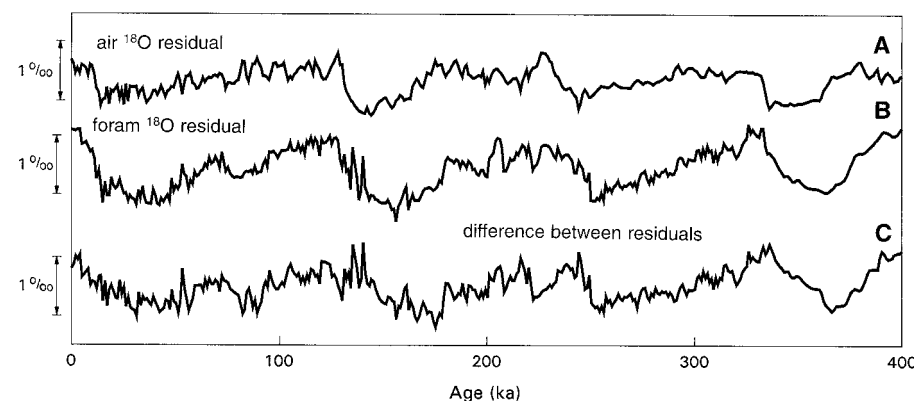


Fig. 3. Components of the $\delta^{18}\text{O}$ records not explained by linear forcing by insolation. (A) The residual obtained by subtracting the Vostok air $\delta^{18}\text{O}$ tuning target from the measured record, attributed to ice volume. (B) The residual obtained by subtracting the V19-30 benthic $\delta^{18}\text{O}$ tuning target from the measured record, attributed to both ice volume and deep-ocean temperature. (C) The difference between these two residuals, attributed to deep-ocean temperature.

Table 1. Spectral analyses of ETP (25) versus tuned air $\delta^{18}\text{O}$ and tuned foraminiferal $\delta^{18}\text{O}$, carried out to evaluate the linearly forced components of the two records (41). Confidence limits for phase lags are at the 95% level.

Forcing	Air $\delta^{18}\text{O}$					Foraminiferal $\delta^{18}\text{O}$				
	Total amplitude (%)	Coherent amplitude		Phase lag		Total amplitude (%)	Coherent amplitude		Phase lag	
		%	Coherency	Deg.	ky		%	Coherency	Deg.	ky
Obliquity	0.29	0.27	0.95	66 ± 15	7 ± 2	0.40	0.39	0.98	62 ± 9	7 ± 1
Precession	0.39	0.39	0.99	79 ± 7	4.6 ± 0.4	0.23	0.21	0.93	61 ± 19	3.6 ± 1.1

the assumptions involved in the tuning (17). When Martinson *et al.* (10) explored the uncertainties in their age model, they were working with geological data sets containing a much larger and irreducible proportion of variance that could not be explained by linear forcing; therefore, they were obliged to attach a rather large uncertainty (an average of 5 ky) to their age estimates. The age model for Vostok air $\delta^{18}\text{O}$ could not be varied by more than ~ 2 ky without substantially reducing the amount of variance representing a linear response.

Exploring the 100-ky signal of the Vostok atmospheric CO₂ records. A long record of atmospheric CO₂ has been obtained from the Vostok core, and it has been noted that its variance is dominated by eccentricity (13). Because the new time scale refers to the air bubbles, it can be directly applied to the CO₂ record (Fig. 4F). With this time scale, the earlier observation is confirmed: The record has a coherence of 0.92 with the 100-ky component of eccentricity and is essentially in phase, and the coherent amplitude of the 100-ky CO₂ signal is equivalent to 30 parts per million by volume (ppmv). At obliquity, the coherence is 0.94, and the coherent amplitude of the signal is equivalent to 16 ppmv, with about the same phase as the $\delta^{18}\text{O}$ signals.

The residual from the Vostok air $\delta^{18}\text{O}$ signal, after subtracting the linearly forced part of the record, is interpreted in terms of

change in the $\delta^{18}\text{O}$ of the ocean. To a first approximation, it should represent the total of that part of the ocean $\delta^{18}\text{O}$ ("ice volume") variability that is not linearly forced by obliquity or precession (Fig. 3A). At a period of 100 ky, this residual signal is highly coherent (0.99) with the Vostok CO₂ signal but lags CO₂.

The residual in the V19-30 foraminiferal $\delta^{18}\text{O}$ signal, after subtracting the linearly forced part (Fig. 3B), must contain contributions from global ice volume and from changing deep-ocean temperature. Thus, to obtain the component of the ocean temperature record that is not linearly forced, I subtracted the Vostok residual (ice volume) from the V19-30 residual (ice volume and temperature), taking account of the 1-ky lag of the air $\delta^{18}\text{O}$ record (Fig. 3C). The coherent amplitude of this record at the 100-ky period is 0.26‰, equivalent to $\sim 0.7^\circ\text{C}$ in temperature. Deep-water temperature is also highly coherent (0.97) with the Vostok CO₂ signal in the 100-ky band. The coherences and phases in the 100-ky band strongly suggest that atmospheric CO₂ has a direct and immediate control on deep-water temperature (presumably with high-latitude air temperature as an intermediary). In addition, temperature has a direct control on ice volume, mediated by the long response times of ice sheets.

It could be argued that the data equally support a model whereby deep temperature has a direct and immediate control over the concentration of CO₂ in the atmosphere. However, it is hard to envisage a mechanism for generating a 100-ky deep-water temperature cyclicity directly, whereas the global carbon system that controls atmospheric CO₂ includes components with long time constants, a necessary requirement for generating a 100-ky signal from the orbital forcing. In either case, the important conclusion that may be drawn from the examination of the 100-ky part of the variance in the several signals is that the prevalent 100-ky signal does not arise from the long time constant of ice volume response. Instead, ice volume responds, with an appropriate lag that is consistent with the value derived by Imbrie and Imbrie (5), to forcing at 100 ky by temperature (it can be assumed that the temperature of the deep ocean also reflects in some way the air temperature at high latitudes).

Important support for this interpretation comes from the Vostok ice D/H record, which is thought to reflect high-latitude temperature in the air over Vostok. Assigning a time scale to the ice itself poses additional problems that are not addressed here, because the ice-air age difference varies from ~ 2 ky at times of higher temperature and accumulation rate to 6 ky or more at cold times when snow accumulation is low. The usual procedure is to derive a time scale for the ice and then compute a time-dependent air-ice age difference that takes account of the temperature and accumulation rates as a function of time. Here, the primary time scale has been developed for the trapped air, so a complex iteration would be required to formally derive an ice time scale. Instead, the ice time scale (13) is simply offset by the same amounts as the gas time scale was changed (Fig. 4E). Although this will slightly affect the high-frequency portion of the variance spectrum, it will not substantially affect the 100-ky signal. This signal has a phase similar to that of the deep temperature record and a coherent D/H amplitude at the 100-ky period of 15‰, equivalent to an air temperature of $\sim 3^\circ\text{C}$.

Testing the partitioning of the $\delta^{18}\text{O}$ signal. On the basis of the argument above, the $\delta^{18}\text{O}$ record of global ice volume may be reconstructed from three components: the precession component, from the coherent precession component of the V19-30 foraminiferal $\delta^{18}\text{O}$ tuning target; the obliquity component, from the coherent obliquity component of the Vostok air $\delta^{18}\text{O}$ tuning target; and the nonlinear residual that is obtained by subtracting the Vostok air $\delta^{18}\text{O}$ tuning target from the measured record (27). This recon-

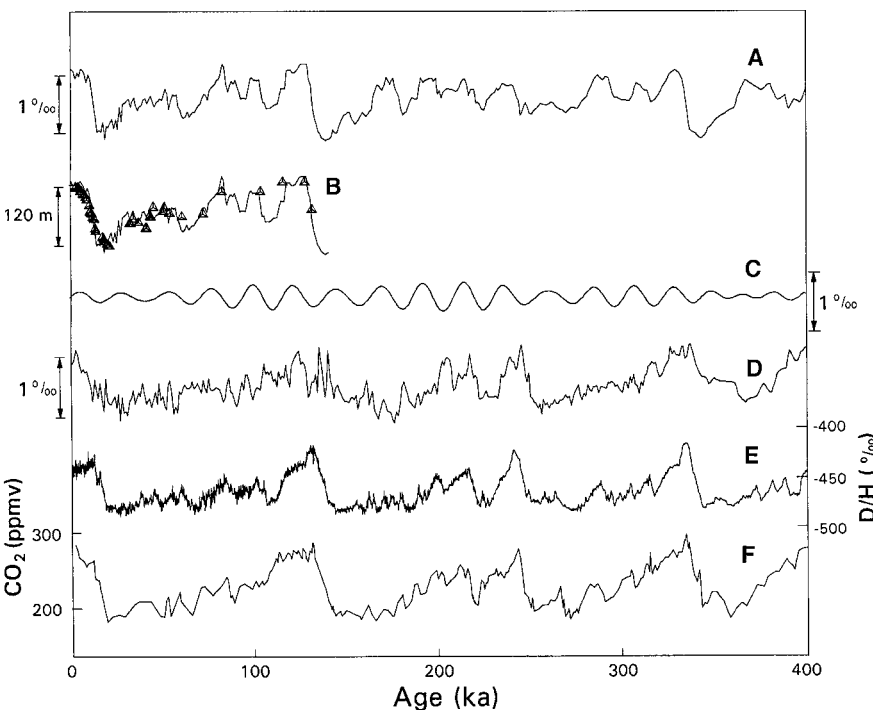


Fig. 4. (A) The reconstructed ocean water $\delta^{18}\text{O}$ record attributable to ice volume and sea level changes. (B) The reconstructed ocean water $\delta^{18}\text{O}$ record (150 ky), scaled as sea level and compared with sea level observations (32). (C) The reconstructed record of changes in the Dole effect. (D) The reconstructed component of foraminiferal $\delta^{18}\text{O}$ attributable to changes in deep-Pacific water temperature. (E) The record of atmospheric CO₂ (13) on the time scale of this paper. (F) Vostok D/H (13) on the time scale of this paper.

struction is illustrated in Fig. 4A. Two aspects of this reconstruction support its being a better reconstruction of ice volume and sea level from $\delta^{18}\text{O}$ than has been previously achieved. First, the ice volume contribution to the difference between the Last Glacial Maximum and the Holocene is $\sim 1.0\%$, close to the reconstruction of $1.0 \pm 0.1\%$ by Schrag *et al.* (28) based on direct measurement of the $\delta^{18}\text{O}$ of relict glacial pore water [also compare estimates in (29) rather than the 1.2% (2), 1.26% (30), or 1.4% (31) estimates based on earlier interpretations of marine isotope records]. Second, the record is consistent with recent sea level estimates (32), as shown in Fig. 4B.

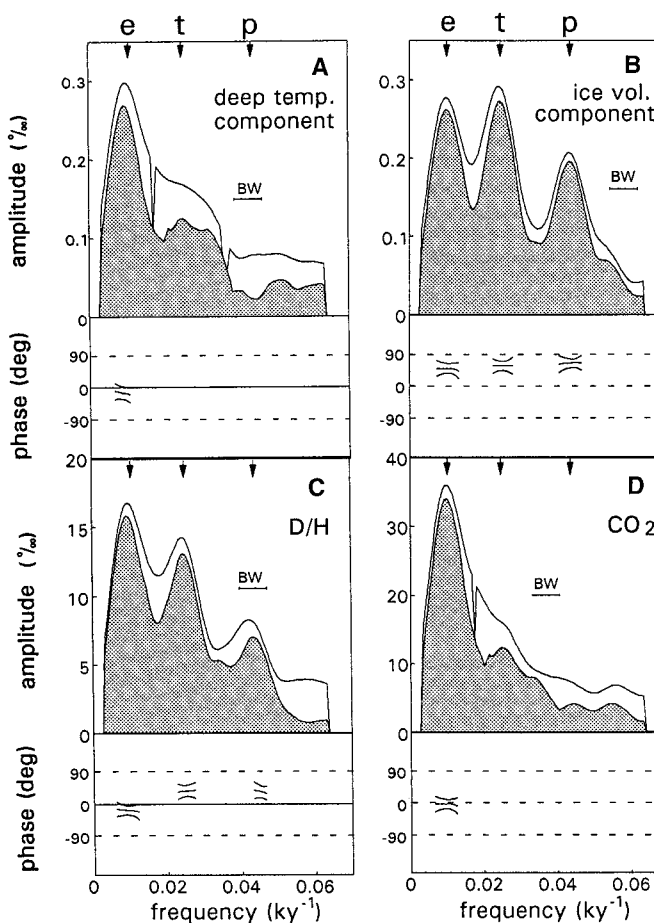
With the derived history of the ice volume component of the foraminiferal $\delta^{18}\text{O}$ record, the total temperature component may be ob-

tained by subtraction as mentioned above. The resulting record is illustrated in Fig. 4D. Figure 5 shows the total amplitude and coherent amplitude spectra of ice volume (Fig. 4A), Pacific temperature (Fig. 4D), Antarctic air temperature (Fig. 4E), and atmospheric CO_2 (Fig. 4F), together with their estimated phases relative to ETP (25). Table 2 summarizes the statistical description of the 100-ky signal in the four records. The CO_2 and deep-ocean temperature records are dominated by variance with a 100-ky period and vary in phase with eccentricity. Contrary to previous interpretations, global ice volume does lag changes in orbital eccentricity, but eccentricity is not the dominant peak in the ice volume spectrum (33). The effect of orbital eccentricity probably enters the paleoclimatic record through an influence on the concentration of atmospheric CO_2 .

Table 2. Spectral analyses (41) to investigate the 100-ky signal in geological records (Fig. 5). Confidence limits for phase lags are at the 95% level. For an explanation of the ETP used, see (25).

Comparison	100-ky coherency	Total 100-ky amplitude	Coherent 100-ky amplitude	Phase lag at 100 ky	
				Deg.	ky
ETP versus deep temperature	0.94	0.30%	0.27% (0.7°C)	-16 ± 18	-5 ± 5
ETP versus CD_2	0.96	36 ppmv	34 ppmv	-4 ± 13	-1 ± 4
ETP versus Vostok D/H	0.97	17%	16% (3°C)	-18 ± 13	-5 ± 4
ETP versus ice volume	0.96	0.28%	0.26%	49 ± 15	14 ± 5

Fig. 5. Linear variance spectra obtained by cross-spectral analysis versus ETP (25) of (A) deep-Pacific temperature, (B) ocean $\delta^{18}\text{O}$ (ice volume, sea level), (C) Vostok D/H (Antarctic air temperature), and (D) Vostok atmospheric CO_2 . In each panel, the top section shows the amplitude and (shaded area) coherent amplitude spectrum, and the bottom shows phases (with 95% confidence limits) for each orbital band (using the convention where a positive phase angle is a measure of the lag in degrees with reference to ETP, that is, with reference to insolation in the Northern Hemisphere midsummer). Arrows labeled "e," "t," and "p" identify the frequencies associated with eccentricity, obliquity (tilt), and precession. The bar labeled "BW" indicates the bandwidth.



References and Notes

- W. S. Broecker and J. van Donk, *Rev. Geophys. Space Phys.* **8**, 169 (1970).
- N. J. Shackleton and N. D. Opdyke, *Quat. Res.* **3**, 39 (1973).
- N. J. Shackleton, *Nature* **215**, 15 (1967).
- J. Imbrie *et al.*, *Paleoceanography* **8**, 699 (1993).
- J. Weertman, *J. Glaciol.* **38**, 145 (1964).
- J. Imbrie and J. Z. Imbrie, *Science* **207**, 943 (1980).
- R. A. Muller and G. J. MacDonald, *Nature* **377**, 107 (1995).
- J. D. Hays, J. Imbrie, N. J. Shackleton, *Science* **194**, 1121 (1976).
- J. Imbrie *et al.*, in *Milankovitch and Climate*, A. Berger *et al.*, Eds. (Reidel, Hingham, MA, 1984), pp. 269–305.
- D. G. Martinson *et al.*, *Quat. Res.* **27**, 1 (1987).
- M. Bender, T. Sowers, L. Labeyrie, *Global Biogeochem. Cycles* **8**, 363 (1994).
- J. R. Petit *et al.*, *Nature* **399**, 429 (1999).
- There is no established protocol for inserting age control points in a glaciological age model for an ice sheet, and the matter is further complicated if the age controls are assigned to the gas record rather than to the solid ice record. The procedure used here is to insert age controls into the time scale of (13) so as to modify it. This clearly gives rise to stepwise changes in the age-depth profile. With only a single ice core, it cannot be determined whether these should be interpreted as changes in snow accumulation, as changes in the thinning function related to the underlying topography, or as a combination of the two.
- D. A. Meese *et al.*, *J. Geophys. Res.* **102**, 26411 (1997).
- M. L. Bender, B. Malaize, J. Orchardo, T. Sowers, J. Jouzel, in *Mechanisms of Global Climate Change at Millennial Time Scales*, P. U. Clark, R. S. Webb, L. D. Keigwin, *Eds.*, vol. 112 of *Geophysical Monograph Series* (American Geophysical Union, Washington, DC, 1999), pp. 149–164.
- Web table 1, data and figures illustrating the earlier steps in the age model development, and other data are available as supplemental material at www.sciencemag.org/feature/data/1052268.shl.
- N. J. Shackleton and N. G. Pisias, in *The Carbon Cycle and Atmospheric CO_2 : Natural Variations Archaeon to Present*, E. T. Sundquist and W. S. Broecker, *Eds.*, vol. 32 of *Geophysical Monograph Series* (American Geophysical Union, Washington, DC, 1985), pp. 303–317.
- D. Ninkovich and N. J. Shackleton, *Earth Planet. Sci. Lett.* **27**, 20 (1975).
- On average, our ages are ~ 2 ky older than those according to the time scale of (9).
- J. Imbrie *et al.*, *Paleoceanography* **7**, 701 (1992).
- A precession-related variation in the Dole effect was also derived in (71), but by a different approach whereby deep-ocean temperature varied in a prescribed manner.
- T. J. Crowley and G. R. North, *Paleoclimatology* (Oxford Univ. Press, New York, 1991), p. 90.
- The strategy for separating a linearly forced component of a paleoclimatic record from a nonlinear residual was pioneered by Imbrie (34) [see also (4)].
- ETP [see (9)] denotes a convenient artificial mix of orbital eccentricity, tilt (obliquity), and precession signals with more or less equal variance and with the phase of midsummer Northern Hemisphere insolation. In view of the shortness of the records considered here, as well as the fact that none of the records under discussion display much low-frequency variance, I have removed the low frequency (400-ky period) of orbital eccentricity variability in constructing the version of ETP used.
- N. G. Pisias, A. C. Mix, R. Zahn, *Paleoceanography* **5**, 147 (1990).
- Another (analytically identical) way of viewing this reconstruction is that it comprises the measured air $\delta^{18}\text{O}$ record with the (modeled) linearly forced non-ice volume component subtracted.
- D. P. Schrag, G. Hampt, D. W. Murray, *Science* **272**, 1930 (1996).
- J.-C. Duplessy, L. Labeyrie, P. L. Blanc, in *Long and Short Term Variations in Climate*, H. Wanner and U. Siegenthaler, *Eds.* (Springer-Verlag, Berlin, 1997), pp. 19–40.

- haler, Eds., vol. 16 of *Lecture Notes in Earth Sciences* (Springer-Verlag, New York, 1988), pp. 83–116.
30. N. J. Shackleton, *Quat. Sci. Rev.* **6**, 183 (1987).
 31. T. J. Crowley and R. K. Matthews, *Geology* **11**, 275 (1983).
 32. Critical age ^{230}Th determinations for MIS 5e are 116 ± 0.9 ka for the end and 128 ± 1 ka for the beginning (35); these have been plotted at a nominal $+6$ m (36). A point at -60 m at 132 ± 2 ka represents the coral at "Aladdin's Cave" (37). Reliable (supported by ^{231}Pa data) ages for MIS 5c (82.8 ± 1.0 ka) and MIS 5c (104.2 ± 1.2 ka) are from Barbados (36, 38). Sea levels during MIS 3 are from the Huon Peninsula, New Guinea (39), and the plotted points for the most recent deglaciation are from offshore Barbados (40).
 33. The amplitude of the 100-ky component in ice volume variability may be even smaller if an account is taken of the effect of changing atmospheric CO_2 pressure (P_{CO_2}) on $\delta^{18}\text{O}$ fractionation in the strato-
 - sphere (11). As suggested in (11), the magnitude of this effect is of the order of 0.4% for today's atmospheric P_{CO_2} , equating to an effect of the order of 0.13% per 100-ppmv change in P_{CO_2} . Because the coherent amplitude of the P_{CO_2} signal at 100 ky is 36 ppmv (Table 2), this correction will reduce the true amplitude of the 100-ky ice volume signal by $\sim 0.047\%$ (from 0.28 to 0.23%). Supplementary material (17) illustrates the effect of making this correction.
 34. J. Imbrie, *J. Geol. Soc. London* **142**, 417 (1985).
 35. C. H. Stirling, T. M. Esat, K. Lambeck, M. T. McCulloch, *Earth Planet. Sci. Lett.* **160**, 745 (1998).
 36. R. K. Matthews, *Quat. Res.* **3**, 147 (1973).
 37. T. M. Esat, M. T. McCulloch, J. Chappell, B. Pillans, A. Omura, *Science* **283**, 197 (1999).
 38. R. L. Edwards, H. Cheng, M. T. Murrell, S. J. Goldstein, *Science* **276**, 782 (1997).
 39. J. Chappell et al., *Earth Planet. Sci. Lett.* **141**, 227 (1996).
 40. E. Bard, B. Hamelin, R. G. Fairbanks, A. Zindler, *Nature* **345**, 405 (1990).
 41. Because the orbital records are not sinusoidal, the estimate of coherent amplitude is not readily used; therefore, tuning targets were created with the same coherent amplitudes empirically. In the precession band, the value given as coherent amplitude is $\sim 38\%$ of the maximum high-to-low range (which occurs between 209 and 220 ky); in the obliquity band, it is $\sim 54\%$ of the maximum high-to-low range (between 212 and 232 ky).
 42. This work was supported by UK Natural Environment Research Council grant GR3/12889. I am very grateful to S. Crowhurst for considerable assistance in data manipulation. I was inspired to tackle the data discussed here by discussions with M. Bender and, more recently, with D. Raynaud. The final manuscript was considerably improved as a consequence of reviews by M. Bender, J. Imbrie, and two anonymous reviewers.

17 May 2000; accepted 31 July 2000

Bacterial Rhodopsin: Evidence for a New Type of Phototrophy in the Sea

Oded Béjà,¹ L. Aravind,² Eugene V. Koonin,²
Marcelino T. Suzuki,¹ Andrew Hadd,³ Linh P. Nguyen,³
Stevan B. Jovanovich,³ Christian M. Gates,³ Robert A. Feldman,³
John L. Spudich,⁴ Elena N. Spudich,⁴ Edward F. DeLong^{1*}

Extremely halophilic archaea contain retinal-binding integral membrane proteins called bacteriorhodopsins that function as light-driven proton pumps. So far, bacteriorhodopsins capable of generating a chemiosmotic membrane potential in response to light have been demonstrated only in halophilic archaea. We describe here a type of rhodopsin derived from bacteria that was discovered through genomic analyses of naturally occurring marine bacterioplankton. The bacterial rhodopsin was encoded in the genome of an uncultivated γ -proteobacterium and shared highest amino acid sequence similarity with archaeal rhodopsins. The protein was functionally expressed in *Escherichia coli* and bound retinal to form an active, light-driven proton pump. The new rhodopsin exhibited a photochemical reaction cycle with intermediates and kinetics characteristic of archaeal proton-pumping rhodopsins. Our results demonstrate that archaeal-like rhodopsins are broadly distributed among different taxa, including members of the domain *Bacteria*. Our data also indicate that a previously unsuspected mode of bacterially mediated light-driven energy generation may commonly occur in oceanic surface waters worldwide.

Retinal (vitamin A aldehyde) is a chromophore that binds integral membrane proteins (opsins) to form light-absorbing pigments called rhodopsins. Rhodopsins are currently known to belong to two distinct protein families. The visual rhodopsins, found in

eyes throughout the animal kingdom (1), are photosensory pigments. Archaeal rhodopsins, found in extreme halophiles, function as light-driven proton pumps (bacteriorhodopsins), chloride ion pumps (halorhodopsins), or photosensory receptors (sensory rhodopsins) (2–5). The two protein families show no significant sequence similarity and may have different origins. They do, however, share identical topologies characterized by seven transmembrane α -helices that form a pocket in which retinal is covalently linked, as a protonated Schiff base, to a lysine in the seventh transmembrane helix (helix G). Recently, a protein with high sequence similarity to the archaeal rhodopsins has also been found in the eukaryote *Neurospora crassa*

(6). The eucaryal rhodopsin formed a photochemically reactive pigment when bound to all-trans retinal and exhibited photocycle kinetics similar to those of archaeal sensory rhodopsins (7). To date, however, no rhodopsin-like sequences have been reported in members of the domain *Bacteria*.

Cloning of proteorhodopsin. Sequence analysis of a 130-kb genomic fragment that encoded the ribosomal RNA (rRNA) operon from an uncultivated member of the marine γ -Proteobacteria (that is, the "SAR86" group) (8, 9) (Fig. 1A) also revealed an open reading frame (ORF) encoding a putative rhodopsin (referred to here as proteorhodopsin) (10). The inferred amino acid sequence of the proteorhodopsin showed statistically significant similarity to archaeal rhodopsins (11). The majority of predicted proteins encoded by ORFs upstream and downstream of the proteorhodopsin gene, as well as the rRNA operon, showed highest similarity to proteobacterial homologs. Given the large amount of apparent lateral gene transfer observed in recent whole genome studies, it is not surprising that some predicted proteins (17 of 74) had significantly greater similarity to those from other bacterial groups, including *Actinomycetes* and Gram-positive bacteria (12, 13). No other ORFs encoding archaeal-like genes, however, were detected in the vicinity of the proteorhodopsin gene, verifying the bacterial origin of the 130-kb genome fragment.

The proteorhodopsin gene encoded a polypeptide of 249 amino acids, with a molecular weight of 27 kD. Hydropathy plots indicated seven transmembrane domains, a typical feature of the rhodopsin protein family, that aligned well with the corresponding helices of the archaeal rhodopsins. The amino acid residues that form a retinal binding pocket in archaeal rhodopsins are also highly conserved in proteorhodopsin (Fig. 2). In particular, the critical lysine residue in helix G, which forms the Schiff base linkage with retinal in archaeal rhodopsins, is present in proteorhodopsin. Analysis of a structural model of proteorhodopsin (14), in conjunc-

¹Monterey Bay Aquarium Research Institute, Moss Landing, CA 95039–0628, USA. ²National Center for Biotechnology Information, National Library of Medicine, National Institutes of Health, Bethesda, MD 20894, USA. ³Molecular Dynamics, Amersham Pharmacia Biotech, Sunnyvale, CA 94086, USA. ⁴Department of Microbiology and Molecular Genetics, The University of Texas Medical School, Houston, TX 77030, USA.

*To whom correspondence should be addressed. E-mail: delong@mbari.org.